nature research
https://doi.org/10.1038/s41566-020-00707-5

Supplementary information

High-power portable terahertz laser systems

In the format provided by the authors and unedited

Supplementary Materials

High power portable terahertz laser systems

Ali Khalatpour[1], Andrew K. Paulsen[1], Chris Deimert[2], Zbig R. Wasilewski[2,3,4,5], and Qing Hu[1]

[1]Department of Electrical Engineering and Computer Science and Research Laboratory of Electronics, Massachusetts Institute of Technology, Cambridge, MA 02139, USA.

[2]Department of Electrical and Computer Engineering, University of Waterloo, 200 University Ave W, Waterloo, Ontario N2L 3G1, Canada.

[3]Department of Physics and Astronomy, University of Waterloo, 200 University Ave W, Waterloo, Ontario N2L 3G1, Canada.

[4]Waterloo Institute for Nanotechnology, University of Waterloo, 200 University Ave W, Waterloo, Ontario N2L 3G1, Canada.

[5]Institute for Quantum Computing, University of Waterloo, 200 University Ave W, Waterloo, Ontario N2L 3G1, Canada.

Materials and Methods

MBE growth

The four quantum cascade laser (QCL) structures were grown with a Veeco GEN10 molecular beam epitaxy (MBE) system. For all four structures, the superlattices (SLs) were grown using a Veeco 60cc conical effusion cell for Al, and a Veeco SUMO v3 cell for Ga. The details of growth conditions specific to THz QCLs have been published elsewhere[1].The Ga and Al cell fluxes were measured before each growth with an ion gauge, which was calibrated regularly by growing dedicated AlAs-GaAs structures and extracting growth rates from high resolution X-ray diffraction (HR-XRD) analysis. To ensure precise control over the layer thicknesses and compositions, the cell fluxes were verified before each growth by growing test layers of AlAs and GaAs on a separate substrate and analyzing in-situ reflectivity oscillations[2].

The growth times for these THz QCL structures can approach 20 hr., which makes effusion cell stability of critical importance. Here, G528, which had the lowest $T_{\max}$ of 192 K, was grown towards the end of an earlier campaign than the other three, with the Ga cell having developed a technical problem. Indeed, HR-XRD measurements of this structure show evidence of GaAs growth rate instability (the lowest trace in Fig. S1). The noticeable splitting of the QCL's higher-order superlattice reflections suggest that Ga flux changed abruptly during the growth by about 1%. Because of that, approximately one quarter of the SL stack was grown at a 1% slower growth rate. On G552, G605, and G652, however, analysis of HR-XRD scans (shown in the same figure) indicate that the cell stabilities were remarkably good, putting an upper bound on the thickness variation of the QCL's 2-well modules at around $\pm 0.2\%$, with the lowest variation for the SL module thickness (G552) close to $\pm 0.05\%$. Fig. S2 shows the omega-2 theta scan for this structure along with a corresponding dynamical simulation.

The superlattice period variations are calculated from the observed broadening of the XRD satellite peak widths. Assuming that the superlattice period varies slowly throughout the stack (e.g., due to Ga flux drift), we expect the full width at half maximum (FWHM) of these peaks to approximately follow $\sqrt{w_0^2 + (2.36 \cdot \sigma\omega)^2}$. Here w_0 is a constant related to instrumental broadening and the finite thickness of the stack, $|\omega|$ is the angular distance of the peak from the main zero-order reflection, and σ is the estimated standard deviation in period thickness. The constant 2.36 scales from standard deviation to FWHM, assuming Gaussian peaks. We extracted the FWHMs by fitting the peaks to a Gaussian shape, then performed least-squares fitting on the series of FWHMs to extract w_0 ($\sim$7 arc sec) and σ for each growth.

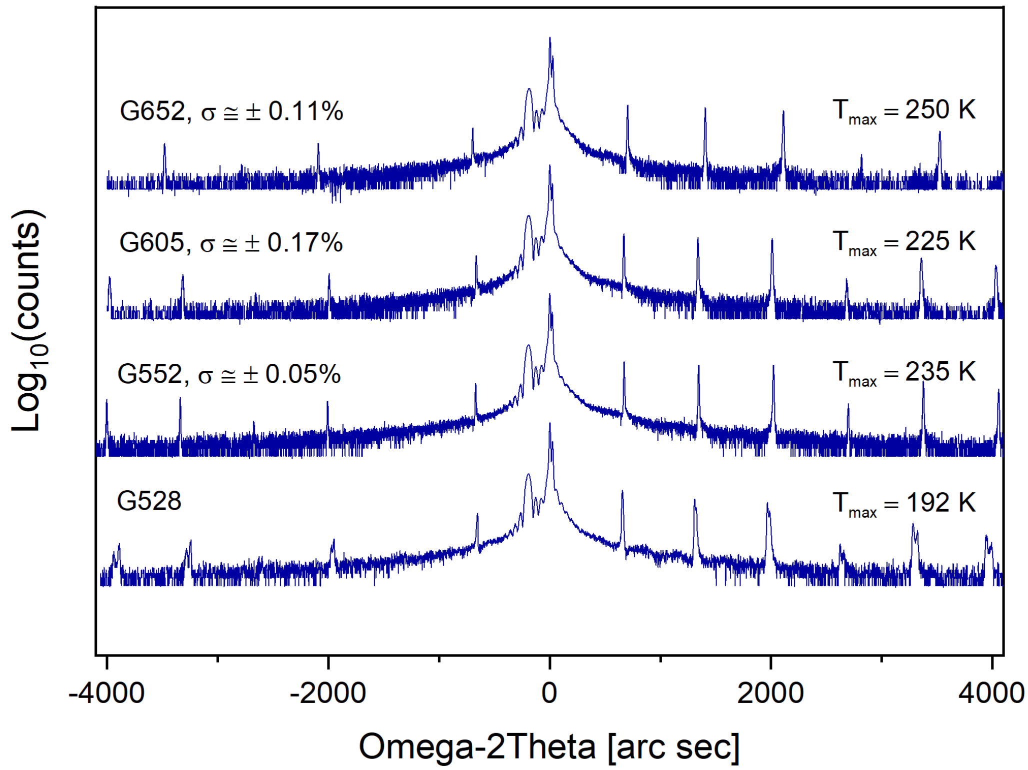

Figure S1: HR-XRD (004) scans for all four structures in logarithmic scale. The scans are displaced by factors of 10^5 for clarity. The σ values quoted are the estimated standard deviation in superlattice period throughout the stack.

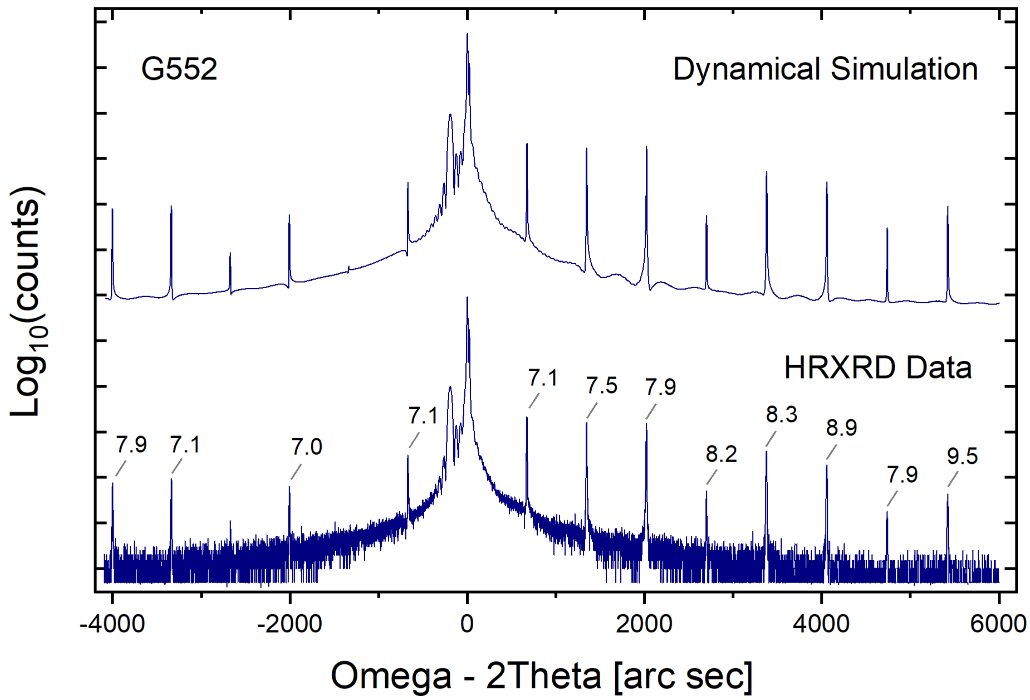

Figure S2: HR-XRD (004) reflection measurement of G552. The dynamical simulation curve has been shifted up for clarity. Peak labels show the FWHM in arc seconds (note the log scale). The FWHM values are obtained by fitting the individual peaks with a Gaussian distribution.

Fabrication

From the MBE wafers, samples of typical size 1.5×1.5 cm^{-2} were cleaved. In addition to the cleaved MBE sample, a slightly larger n+ GaAs substrate (from AXT, Inc.) is necessary; this substrate is named the "receptor," as the MBE growth is transferred to it during the fabrication process. Ta(10 nm)/Au(250 nm) was evaporated onto both the MBE sample and receptor substrate in a ~5×10^{-7} Torr vacuum at a rate of 1 Å/s. The MBE sample and receptor were then bonded together using a metal-metal thermocompression at 300°C and 4 MPa of force for one hour in vacuum. Then the samples were annealed at the same temperature, but in atmospheric pressure nitrogen (N_2) and with no applied force for 45 minutes. Graphite spacers were used to distribute the force uniformly during bonding. Following wafer bonding, the native MBE substrate was lapped down to a thickness of ∼100 μm. This remaining MBE substrate was then removed by wet etching in a 4:1 (by volume) solution of citric acid (1 g/mL) and 20% hydrogen peroxide (H_2O_2), which stops selectively at the $Al_{0.55}Ga_{0.45}As$ etch-stop layer. The exposed etch-stop layer was then selectively removed by concentrated (49%) hydrofluoric acid (HF). The top n+ contact was removed by a solution of H_3PO_4(1)/H_2O_2(1)/ H_2O(25). This completed the transfer of the gain medium epitaxial layer to the receptor substrate. The top contact/waveguide metal was then defined by a bilayer liftoff process (double coating of PGMI-SF5 and SPR700). The final top metallization layer was Ta(10 nm)/Au(250 nm), deposited under the same conditions as the first evaporation. The mesa was then defined through dry-etching in 1/7/30 sccm Cl2:SiCl4:Ar at 1 Pa, for which the top Au acts as a self-aligned mask. The dry etch recipe achieved vertical sidewalls thanks to the formation of a protective Si-based film during the etch. This layer had to be removed to facilitate successful device cleaving. The sidewall passivation was removed by immersion in buffered-oxide etchant (BOE). The receptor wafer was then lapped down to ~190 μm and metalized with Ti(10 nm)/Au(150 nm) at ~ 2×10^{-6} Torr vacuum with a 2 Å/s deposition rate. The overall fabrication process is shown in Fig. S3.

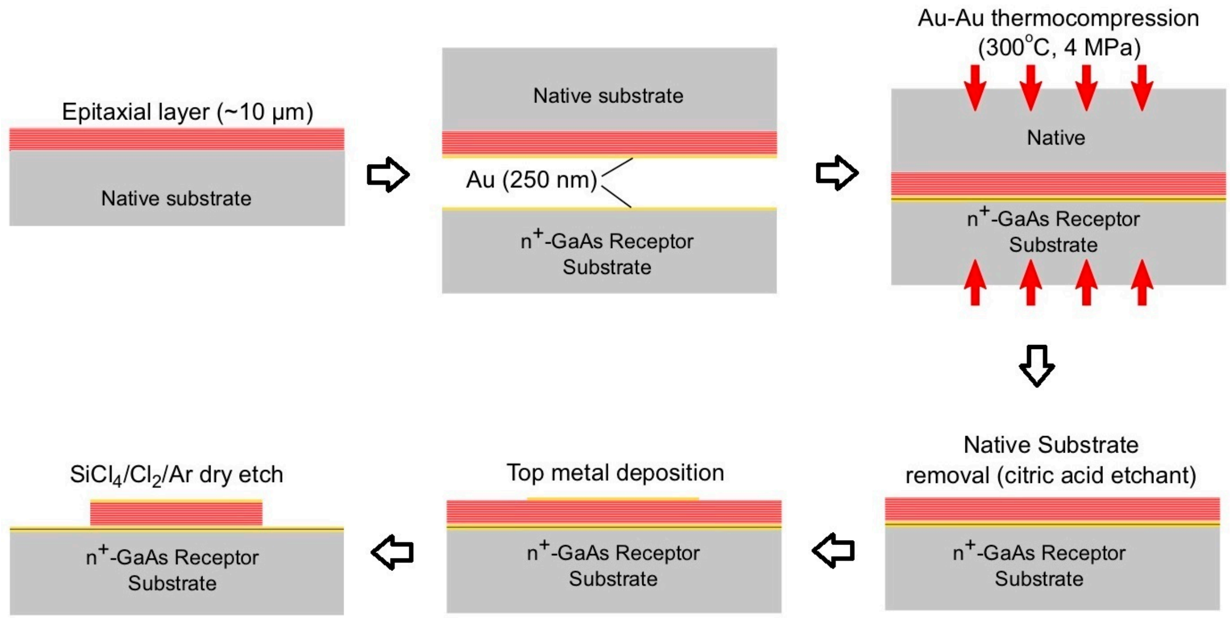

Figure S3: Fabrication process of the THz QCLs in this paper.

Voltage-Current-Light measurement

For the results presented in Fig. 2, the QCL devices were mounted in a closed cycle pulse-tubed helium cooler for measurement (model PT810, built by Cryomech Inc.), which cools down to ~8 K. Characterization was performed using devices of approximate dimensions 1.3 mm × 150 μm. Lasers were biased using an Avtech model AVR-250B pulsed supply. Pulsing conditions were 400 ns at 500 Hz, corresponding to a 0.02% duty cycle. This extremely low duty cycle is typically necessary to avoid device heating and to obtain maximum lasing temperatures. Voltage and current were monitored using a digital oscilloscope (Pico 4824 from Pico

Technology). Voltage measurements were made electrically parallel to the device under test. Current was indirectly sampled using an inductively coupled current sensor (current probe 711S from Integrated Sensor Technology). For optical detection, two instruments were used. For absolute power measurements, a calibrated power meter developed by Thomas Keating Ltd. was used. The average power measured by the meter was then divided by the duty cycle to obtain the peak pulsed power. For L-I measurements, the optical power output was measured using a liquid helium (LHe) cooled Ga-doped Ge photodetector, built by Infrared Laboratories Inc. The uncalibrated power measurement was then scaled to match the absolute power measured by the Thomas Keating meter. Detector noise can mask a small optical signal, so it is essential to use a low-noise detector like the Ge:Ga photodetector for measurements near T_{max}. However, a downside of this detector is that it has a rather limited dynamic range. To overcome this, measurements at low temperature were taken with a perforated anodized aluminum screen to prevent detector saturation. At high temperatures (near $T_{\max}$), the screen was removed to obtain the highest possible sensitivity. At intermediate temperatures, optical measurements were taken both with and without the screen. These intermediate measurements were used to scale the low temperature measurements to the high temperature measurements.

Thermoelectrically cooled laser characterization

With a single-stage TEC cooler (Laird systems, model ZT6-7-F1-3030-TA-W8), a base temperature of 235 K was maintained while removing ~2 W of heat generated by a QCL operated in pulsed mode (at 1% duty cycle). Zinc oxide was used as a thermal paste. The combined heat load of the TEC module and QCL was removed through a copper heat sink and a fan integrated with the vacuum chamber. The assembled chamber is shown in Fig. S3. A closed cycle pulse-tubed helium cooler and an MIT coffee mug are also shown for perspective. The characteristics of the single-stage TEC cooled laser were measured using a room-temperature pyroelectric detector (from QMC Instruments Ltd with a noise equivalent power (NEP) of ~460 $\frac{\mathrm{pW}}{\sqrt{\mathrm{Hz}}}$). Real-time imaging measurements were performed using a NEC IRV-TO831 THz camera (manufactured by NEC with a NEP in the range of ~50 $\frac{\mathrm{pW}}{\sqrt{\mathrm{Hz}}}$) and required much higher average power levels than the spectral measurements made with a pyroelectric detector. Using a three-stage TEC module (Laird systems, model MS3-119-20-15-11-W8) inside the same vacuum chamber, but with an external single-stage TEC module (TE Technology, Inc, model CP-200HT) to stabilize the heatsink temperature, an operating temperature of 210 K was achieved with 2 W heat removal capacity. The overall assembly is shown in Fig. S5A.

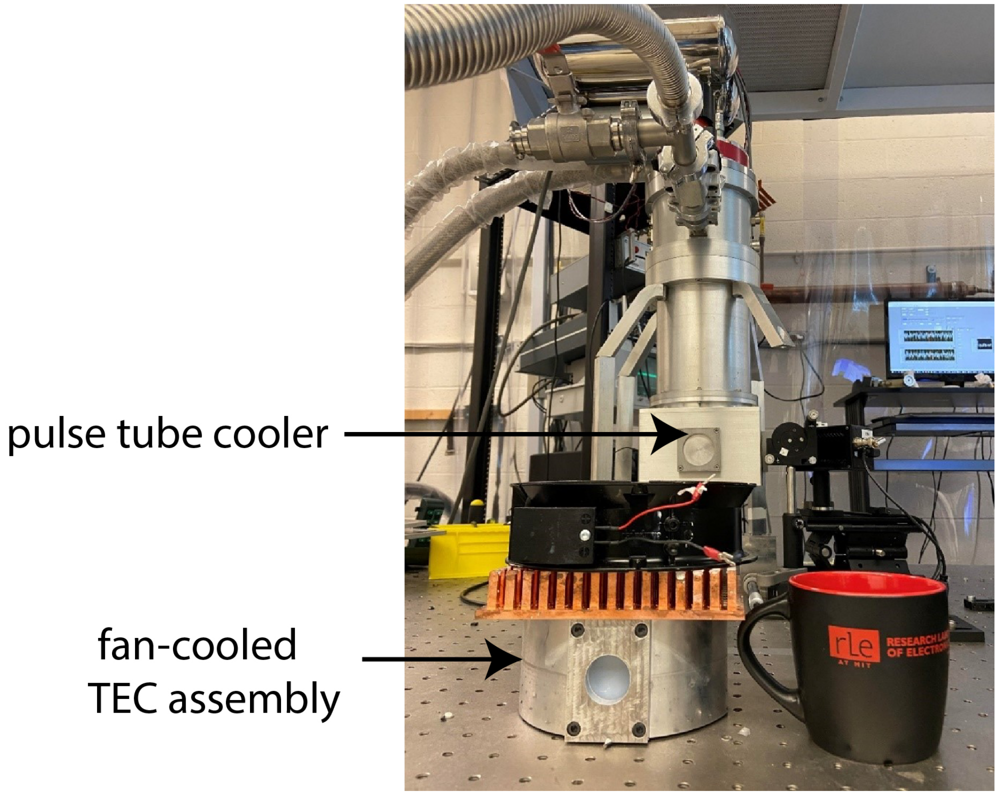

Figure S4: Single-stage fan-cooled TEC assembly with 4.5” diameter and 6” height. A pulse tube cooler that is commonly used in a laboratory environment is also shown in the background without showing the required pumps and Helium compressor. The spacing of holes on the optical table is 1 inch.

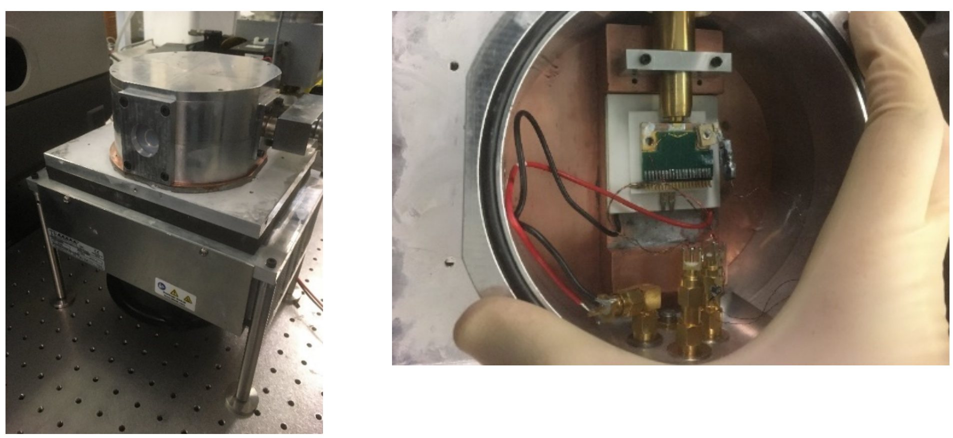

a **b**

Figure S5: Four-stage TEC with 3 stages inside a vacuum chamber and a single stage outside to stabilize the heat-sink temperature. **a**, An exterior picture of the final assembly. **b**, QCL chip and an outcoupling Winston cone is shown. The spacing of holes on the optical table is 1 inch.

Band structure calculation

The most fundamental tool in the design of THz QCL structures and analysis is a numerical package to calculate subband wavefunctions and energies. In this paper, the *k·p* method is employed to calculate the electronic states in semiconductor heterostructures based on the envelope function description. Inclusion of non-parabolicity via *k·p* is crucial for the optimization of these structures due to high electric field at injection alignment – neglecting it can lead to errors comparable to injection anticrossing ($\Omega_{i,u}$). Within the *k·p* framework, the electronics states can be described by the 8-band Kane Hamiltonian (which includes conduction, light-hole, heavy-hole, and split-off bands and their spin interactions). Here we follow the formulation in ref[3]. Assuming that z is the growth direction of quantum wells, with the approximation that in-plane momentum vector is negligible $k_x, k_y \approx 0$, the heavy-hole band is decoupled from the other valance bands. This results in two equivalent 3×3 Hamiltonians for each spin configurations. After these simplifications, the Hamiltonian reads as:

$$\hat{H} = \begin{pmatrix} E_c(z) & \sqrt{\frac{2}{3}}\frac{p_{cv}}{m_0}\hat{p}_z & -\sqrt{\frac{1}{3}}\frac{p_{cv}}{m_0}\hat{p}_z \\ -\sqrt{\frac{2}{3}}\frac{p_{cv}^*}{m_0}\hat{p}_z & E_{lh}(z) & 0 \\ \sqrt{\frac{1}{3}}\frac{p_{cv}^*}{m_0}\hat{p}_z & 0 & E_{so}(z) \end{pmatrix} \qquad \hat{p}_z = -i\hbar\frac{\partial}{\partial z}$$

This Hamiltonian acts on an envelope vector $\chi = (\chi_c, \chi_{lh}, \chi_{so})$. Here *c*, *lh*, and *so* label the conduction, light-hole, and split-off band edges respectively. With further simplification, χ_c can be derived as follows:

$$\hat{p}_z \frac{1}{2m(E,z)}\hat{p}_z\chi_c + E_c(z)\chi_c = E\chi_c \, .$$

In which

$$\frac{1}{m(E,z)} = \frac{1}{m_0}\left[\frac{2}{3}\frac{E_p}{E+E_g} + \frac{1}{3}\frac{E_p}{E+E_g+E_{so}}\right]$$

$$E_p(x) = \frac{3m_0}{m^*(x)}\left[\frac{2}{E_g(x)} + \frac{1}{E_g(x)+E_{so}(x)}\right]^{-1}$$

$$m^*(x) = m_0\left(0.067\left(1-x\right)+0.15x\right)$$

$$E_{so}(x) = 0.341(1-x)+0.28x\ eV$$

$$p_{cv}(x) \ = \ \mathrm{i}\sqrt{\frac{m_0 E_p(x)}{2}}$$

$$E_c(x) = CBO \times (E_g(x) - 1.515)$$

Here, CBO is the conduction band offset, E_g is the bandgap, m_0 is the bare electron mass, and $x = 0.3$. An accurate estimation of band structure requires both E_p and E_c. E_c only depends on the product of bandgap and the conduction band offset. However, E_p depends directly on E_g. To improve the accuracy of our band structure computations, we accounted for the fact that in THz QCLs with two-well active regions, the alignment of the levels is very sensitive to the conduction band offset in the heterostructure of $Al_{0.3}Ga_{0.7}As/GaAs$, and there is no unanimous agreement on the value[4,5,6]. Since the lasing frequency can be measured accurately and lasing occurs at the alignment of the injector to the upper level, we used experimental data on lasing frequencies from a dozen previously grown structures as a figure-of-merit to train a machine-learning model on the band offset for $Al_{0.3}Ga_{0.7}As/GaAs$. The band gap parameters that were reported in the work[4] and the fitted band offset of 72 % provided the best predictive results for the lasing frequencies (with < 2% error). The resulting 1D Schrödinger equation was then solved with a shooting method algorithm.

Design and optimization

A useful design tool for minimization of relevant parasitic channels is an anticrossing graph and the anticrossing curves are shown in Fig. S7, which corresponds to Fig.1 in the main text. This graph shows the level alignments over a wide range of module biases. Minima in anticrossing correspond to a resonant alignment of two levels in energy, and the anticrossing gap is a measure of the coupling strength between those two levels. Because of a strong dephasing rate of ~4 meV (corresponding to 1 THz linewidth), the coupling between two levels with anticrossing gap <0.5 meV is insignificant. In general, those levels that align closer to the $|i_{n-1}\rangle \to |u_n\rangle$ alignment will negatively impact a "clean" 3-level system. The main parasitic channels beside $|i_{n-1}\rangle, |u_n\rangle \to |p_{1,2,n}\rangle$ are $|i_{n-1}\rangle, |u_n\rangle \to |p_{2,n+1}\rangle$, and $|l_n\rangle \to |p_{1,n+1}\rangle$.

Here we formulate our optimization problem as the following: $X = [x_1, x_2, x_3, x_4]^T$ is a vector that represents all the barrier and well thicknesses, and the voltage drop per module is denoted by *V*. The anticrossing gap and the alignment bias between levels $|i\rangle$ and $|j\rangle$ are defined as;

$$V_{i,j}(X) = \arg\ \min\left(\left|E_i(X,V) - E_j(X,V)\right|\right).$$
$$\Omega_{i,j}(X) = \left|E_i(X,V_{i,j}(X)) - E_j(X,V_{i,j}(X))\right|.$$

Here $E_i(X,V)$ is the energy of level $|i\rangle$ at the geometry parameters of *X* and at bias *V*. The figure of merit in our optimization problem is

$$X_{opt} = \arg\ \min\left(-N_{i,pp}E_{i,pp}(X,V_{i,u}(X)) + N_{i,pp}^{W} f_{i,pp}(X,V_{i,u}(X)) - N_V\left(V_{l,p_{1,n+1}}(X) - V_{i,u}(X)\right)^2\right),$$
$$V_{design} = V_{i,u}(X_{opt}).$$

Subject to;

$$
\begin{aligned}
&0.28 \le f_{u,l}(X, V_{i,u}(X)) \le 0.32, \\
&15.5 \text{ meV} \le E_u(X, V_{i,u}(X)) - E_l(X, V_{i,u}(X)) \le 16.5 \text{ meV}, \\
&\Omega_{i,u}^{\min} \le \Omega_{i,u}(X) \le \Omega_{i,u}^{\max}, \\
&E_{ex}(X, V_{i,u}(X)) \le E_{ex}^{\max}, \\
&\Omega_{i_{n-1}, p_{2,n+1}}(X),\ \Omega_{u_n, p_{2,n+1}}(X) \le 0.5 \text{ meV}, \\
&\Omega_{l_n, p_{1,n+1}}(X) \le 0.9 \text{ meV}.
\end{aligned}
$$

Here, $f_{u,l}$ is the oscillator strength between upper and lower lasing level and is defined as:

$$f_{u,l} = (\frac{2m^*_{GaAs}e}{\hbar^2})(E_u - E_l)\left|\left\langle \chi_c^u(z) | z | \chi_c^l(z) \right\rangle + \left\langle \chi_{lh}^u(z) | z | \chi_{lh}^l(z) \right\rangle + \left\langle \chi_{so}^u(z) | z | \chi_{so}^l(z) \right\rangle\right|^2$$

Here, -e is the electron charge, $E_{ext} = E_{l_n} - E_{i_n}$, and $\left[N_{i,pp}, N_{i,pp}^W, N_V \right]$ are normalization factors. $f_{i,pp}$ is the oscillator strength between $\left| i_{n-1} \right\rangle$and $\left| p_{1,n} \right\rangle$ and is defined in the same way as $f_{u,l}$. The resulting optimization problem was solved using MATLAB fminsearch which is based on a simplex algorithm.

Note that the oscillator strength is a convenient quantity for optimization because it is related to the scattering rate. This can be qualitatively understood by the expansion of a general perturbation Hamiltonian in Fermi's golden rule using Taylor expansion. Assume a position dependent perturbation $H'(z)$ and the matrix element $A_{u,l}$ between $\left| u \right\rangle and \left| l \right\rangle$ which reads as:

$$\left| A_{u,l} \right|^2 = \left| \int \psi_u(z)\ H'(z)\ \psi_l^*(z) dz \right|^2$$

Expanding the $H'(z)$ in Taylor expansion to the first order results in:

$$\left|A_{u,l}\right|^2 \approx \left|\int \psi_u(z)\ (1+qz)\ \psi_l^*(z)dz\right|^2 = \text{constant } \times f_{u,l}$$

This approximation is similar to small momentum exchange in the LO-phonon scattering matrix element. In this case, by expanding $H'(z)$ based on its Fourier transform, we can write:

$$\left|A_{u,l}(q)\right|^2 = \left|\int \psi_u(z) e^{iqz} \psi_l^*(z)dz\right|^2$$

For small momentum exchange that is favored in *LO*-phonon scattering near resonance, we can use the same approximation in Taylor expansion and approximate $\left|A_{u,l}(q)\right|^2$ as:

$$\left|A_{u,l}(q)\right|^2 \leq \left|q\right|^2 \left|\int \psi_u(z)\ z\ \psi_l^*(z)dz\right|^2 = \text{constant} \times f_{u,l}$$

Therefore, by minimization of oscillator strength, we also indirectly minimize scattering through other mechanisms.

The anticrossing graph in Fig. S8 shows that the optimization bounds $\Omega_{i_{n-1},p_{2,n+1}}(X),\ \Omega_{u_n,p_{2,n+1}}(X) \leq 0.5\ \text{meV}$ were met for all designs. However, As illustrated in Fig. S8, for G605, $\Omega_{1_n,p_{1,n+1}}(X) > 1\ \text{meV}$ and $V_{l_n,p_{1,n+1}} - V_{i,u}$ was reduced compared to G552. Increasing $V_{l_n,p_{1,n+1}} - V_{i,u}$ cause higher $E_{p_{1,n+1}} - E_{l_n}$ at $V_{i,u}$ (7.4 meV for G552 and 6.7 meV for G605). An appreciable depopulation of lower lasing level with any other channels besides direct LO-phonon depopulation will break the clean 3-level system and should be minimized.

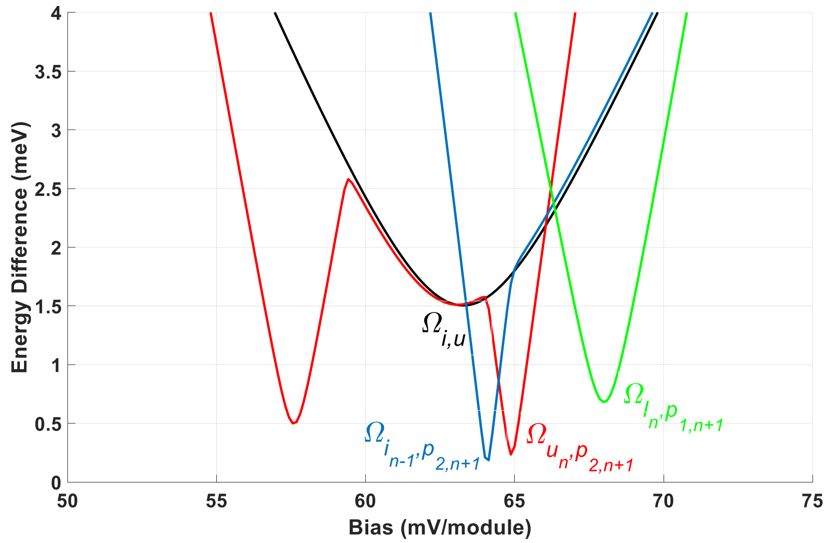

Figure S7: Anticrossing graph highlighting three parasitic channels $|i_{n-1}\rangle, |u_n\rangle \rightarrow |p_{2,n+1}\rangle$, $|l_n\rangle \rightarrow |p_{1,n+1}\rangle$.

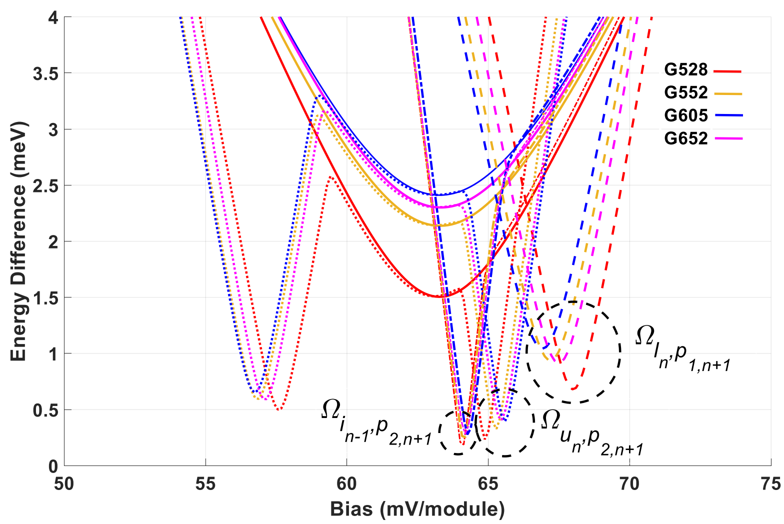

Figure S8: Anticrossing graph for the four grown wafers.

<u>On threshold current density and lasing frequency:</u>

The designs in this work, while achieving record-high $T_{\max}$, have a practical downside in that they have a large intrinsic current leak. In THz QCLs with two-well active region, such as these, the injection barrier is the only barrier that separates the injector from both the upper lasing level and the lower lasing level. Therefore, increasing the injection anticrossing leads to an increase in the parasitic current density when the injector is aligned with the lower lasing level. This parasitic channel, as shown in Figure S9 labeled $\Omega_{i,l}$, sets the lower bound of the threshold current density. To improve the injection efficiency, higher energy spacing and reduced oscillator strength between the upper and lower lasing levels were used.

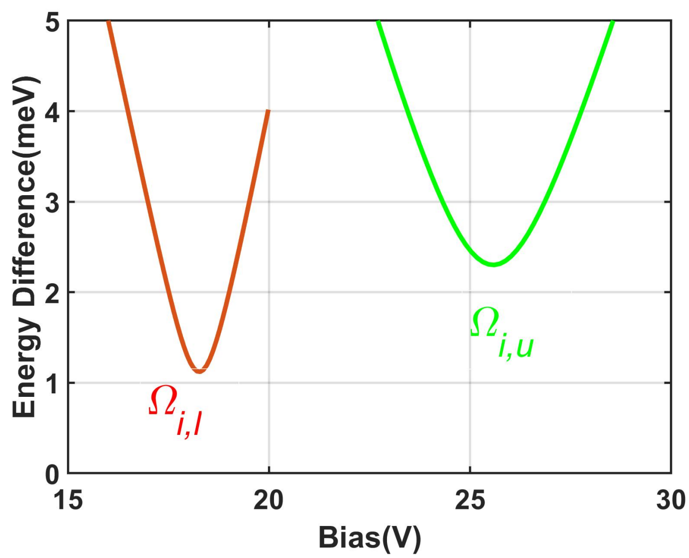

Figure S9: Anticrossing graph for G652. Only the anticrossing between the injector and the upper and lower lasing levels are shown.

The lasing spectra for G652 measured at ~12 K are shown in Figure S10. The distinctive two lasing frequencies suggest double peaks in the gain medium. The spacing between the two peaks is ~0.5 THz which matches well with the injection anticrossing of 2.3 meV (corresponding to 0.56 THz) for G652. This behavior could explain the mode hopping and consequently change in the slope efficiency in the L-I graphs shown in both Figure 2a and Figure 3a in the main text.

As it is shown in Figure S10, at ~ 4 .1A (2150 A/cm^2), a mode appears at 3.4 THz. Due to lower collection efficiency and lower slope efficiency, this could be a higher order lateral mode.

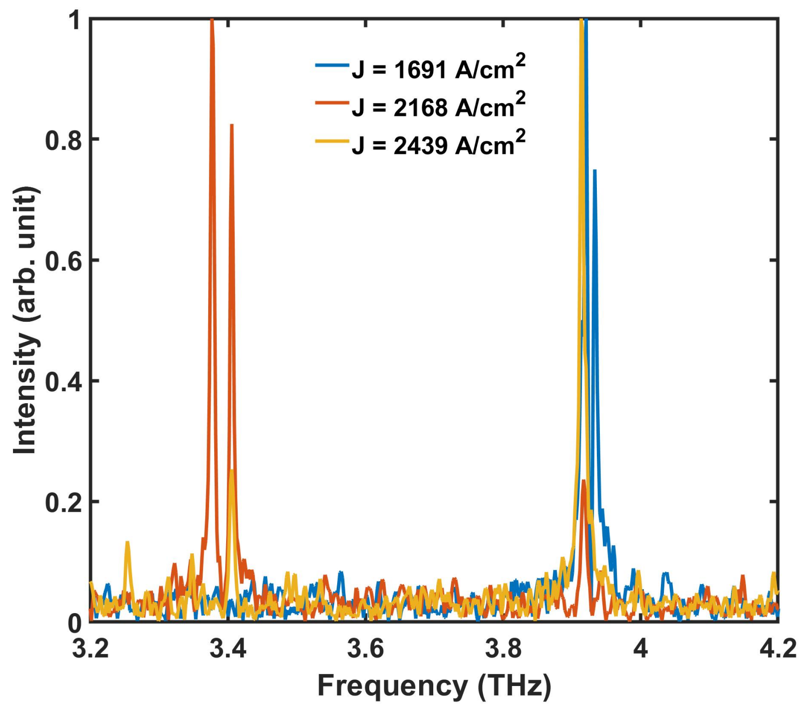

Figure S10: Lasing spectrum for G652 at different current injection, measured at 12 K.

<u>Spectral measurements:</u>

The spectra shown in Figure 2b inset is taken at 246 K with Nicolet 8700 FTIR and a liquid helium cooled Ge:Ga photodetector as the detector. After optical alignment and possible atmospheric loss due to long optical path, the photodetector output signal was ~10 mV, which was measured with an oscilloscope and correspond to the lasing spectra shown in Figure 2b inset. Figure S11 shows the photodetector response when the detector is placed directly at the pulse tube cooler exit window. This ensures maximum detection from the device. Though we have not provided the spectra closer to T_{max} =250 K due to weak optical power for T>246 K, the photodetector output signal for G652 close to the T_{max} = 250 K is still >10 mV and is higher than the signal level used to measure the spectra at 246 K. Figure S11 also shows the threshold behavior in photodetector response. No signal was observed at $T > T_{max} = 250$ K.

The spectra shown in Figure 3a inset is taken with Nicolet 8700 FTIR and using a room-temperature pyroelectric detector (from QMC Instruments Ltd with a noise equivalent power (NEP) of ~460 $\frac{\mathrm{pW}}{\sqrt{\mathrm{Hz}}}$) at 235 K.

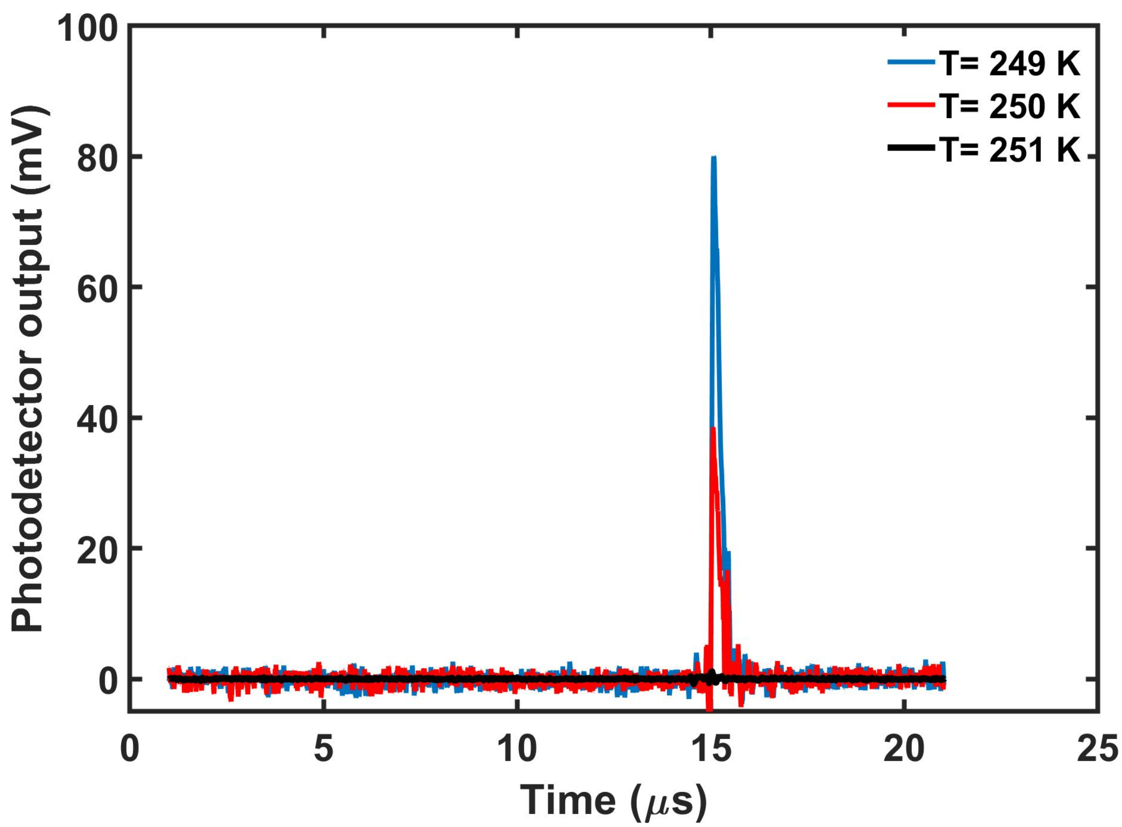

Figure S11: Lasing behavior of G652 close to the $T_{max} = 250$ K.

References

1. Wasilewski, Z. R. MBE growth of THz quantum cascade lasers. in Molecular Beam Epitaxy from research to mass production. 631-655 (*Elsevier*, 2013).
2. Breiland, W. G. & Killeen, K. P. A. virtual interface method for extracting growth rates and high temperature optical constants from thin semiconductor films using *in situ* normal incidence reflectance. *J. Appl. Phys.* **78**, 6726-6736 (1995).
3. Sirtori, C., Capasso, F., Faist, J.& Scandolo. S. Nonparabolicity and a sum rule associated with bound-to-bound and bound-to-continuum intersubband transitions in quantum wells. *Phys. Rev B.* **50**, 8663-8674 (1994).
4. Wasilewski, Z. R., Dion, M. M., Lockwood, D. J.& Poole. P. Composition of AlGaAs. *J. Appl. Phys.* **81**, 1683-1694 (1997).
5. Vurgaftman, I., Meyer, J. A.& Ram-Mohan, L. A. Band parameters for iii–v compound semi-conductors and their alloys. *J. Appl. Phys.* **89**, 5815–5875 (2001).
6. Wang, Y. et al. Band offset of GaAs/AlGaAs heterojunctions from atomistic first principles. *Appl. Phys. Lett*. **102**, 132109 (2013).